The Astrophysical Journal, 618:962–972, 2005 January 10

MICROLENSING DETECTION AND CHARACTERIZATION OF WIDE-SEPARATION PLANETS

Cheongho Han,[1,2] B. Scott Gaudi,[3] Jin H. An,[4] and Andrew Gould[2]

Received 2004 July 20; accepted 2004 September 22

ABSTRACT

With their excellent photometric precision and dramatic increase in monitoring frequency, future microlensing survey experiments are expected to be sensitive to very short timescale, isolated events caused by free-floating and wide-separation planets with masses as low as a few lunar masses. The scientific value of these detections would be greatly enhanced if their nature (bound or unbound) could be accurately characterized and if the planet masses could be measured. Here we present a comprehensive discussion of the ability of microlensing to detect and characterize wide-separation planets. We estimate the probability of measuring the planetary Einstein radius $\theta_{\rm E,}p$ for bound and free-floating planets; this is one of the two additional observables required to measure the planet mass. We carry out detailed simulations of the planetary events expected in next-generation surveys and estimate the resulting uncertainty in $\theta_{\rm E,}p$ for these events. We show that, for main-sequence sources and Jupiter-mass planets, the caustic structure of wide-separation planets with projected separations of $\lesssim$20 AU substantially increases the probability of measuring the dimensionless source size and thus determining $\theta_{\rm E,}p$ compared to the case of unbound planets. In this limit where the source is much smaller than the caustic, the effective cross section to measure $\theta_{\rm E,}p$ to 10% is $\sim$25% larger than the full width of the caustic. Measurement of the lens parallax is possible for low-mass planetary events through combined observations from the ground and a satellite located in an L2 orbit; this would complete the mass measurements for such wide-separation planets. Finally, short-duration events caused by bound planets can be routinely distinguished from those caused by free-floating planets for planet-star separations $\lesssim$20 AU from either the deviations due to the planetary caustic or (more often) the low-amplitude bump from the magnification due to the parent star.

Subject headings: gravitational lensing — planetary systems — planets and satellites: general

Online material: color figures

1. INTRODUCTION

Microlensing experiments were originally proposed to search for Galactic dark matter in the form of massive compact objects (Paczyński 1986). However, microlensing developed several other applications, including the detection and characterization of extrasolar planets (Mao & Paczyński 1991; Gould & Loeb 1992). Recently, Bond et al. (2004) reported the first clear-cut microlensing detection of an exoplanet.

Microlensing planet searches currently operate in the survey/follow-up mode. Large areas of the sky are sparsely monitored by survey collaborations (Alcock et al. 1996; Soszyński et al. 2001; Bond et al. 2002) to detect ongoing microlensing events arising from normal stars. These events are alerted in real time before the event peak and then individually followed up with the dense sampling needed to detect the short-duration (about a day for a Jupiter-mass planet and a few hours for an Earth-mass planet) perturbation to the primary light curve caused by a planetary companion to the primary lens (Albrow et al. 1998; Rhie et al. 2000; Yoo et al. 2004b). One limitation of this type of planet search strategy, however, is that events are only efficiently followed when the source is located within the Einstein ring radius of the primary. Generally, such source positions are only sensitive to planets with separations located within a certain range of distances from their host stars. Planets in this so-called lensing zone have separations in the range of $0.6 \lesssim s \lesssim 1.6$, where s is the projected star-planet separation normalized by the Einstein ring radius. For a typical Galactic bulge event with a lens and a source located at $D_{ol} = 6$ kpc and $D_{os} = 8$ kpc, respectively, the Einstein ring has a radius of

$$r_{\rm E} \sim 2\ {\rm AU}\left(\frac{M}{0.3\ M_\odot}\right)^{1/2}, \qquad (1)$$

where M is the primary-star mass, and thus, current microlensing planet searches are primarily sensitive to bound planets in the range of projected physical separations, $r_\perp$, of $1\ {\rm AU} \lesssim r_\perp \lesssim 5$ AU. Furthermore, because the follow-up is generally done with small field-of-view instruments, the events must be monitored sequentially. As a result, only a few events can be followed at any given time, and it is difficult to achieve the requisite temporal sampling on a sufficient number of events to detect short-duration, low-probability events such as those caused by low-mass or large-separation planets.

These limitations can be overcome with the advent of future lensing experiments that will use very large format imaging cameras to survey wide fields continuously at high cadence. These next-generation surveys will dispense with the alert/follow-up mode of searching for planets and instead simultaneously obtain densely sampled light curves of all microlensing events in their field of view. Because all the stars in the field will be monitored continuously regardless of whether they are being lensed or not, planets will be able to be detected at very large projected separations when the primary star is not

[1] Department of Physics, Institute for Basic Science Research, Chungbuk National University, Chongju 361-763, Korea; cheongho@astroph.chungbuk.ac.kr.

[2] Department of Astronomy, Ohio State University, Columbus, OH 43210; gould@astronomy.ohio-state.edu.

[3] Harvard-Smithsonian Center for Astrophysics, 60 Garden Street, Cambridge, MA 02138; sgaudi@cfa.harvard.edu.

[4] Institute of Astronomy, University of Cambridge, Madingley Road, Cambridge CB3 0HA, UK; jin@ast.cam.ac.uk.

significantly magnifying the source, and indeed even when the signature of the primary is absent. Therefore, these surveys are expected to be sensitive to both wide-separation (Di Stefano & Scalzo 1999a, 1999b) and even free-floating (Bennett & Rhie 2002; Han & Kang 2003) planets. Such planet populations are difficult or impossible to probe by other planet search techniques. Several such high-frequency experiments in space and on the ground have already been proposed or are being seriously considered. The proposed space microlensing mission of the *Microlensing Planet Finder* (*MPF*; Bennett & Rhie 2002; Bennett et al. 2004) is designed to continuously monitor $\sim 10^8$ Galactic bulge main-sequence stars with $\sim 1\%$ photometric precision and a frequency of several times per hour by using a 1–2 m aperture space telescope. Detailed simulations of the outcomes of a ground-based high-frequency experiment using a network of 2 m class telescopes are being carried out by B. S. Gaudi et al. (2005, in preparation).

Although efficient in detecting both bound and free-floating planets, the microlensing method suffers the shortcoming that the mass of the detected planet is generally poorly constrained. For events due to bound planets in which the primary is also detected, analysis of the global light curve automatically yields the planet-star mass ratio $q = m_p/M$, but the stellar mass is unknown because of the degeneracy of the physical lens parameters in the principal lensing observable. This degeneracy arises because among the three observables related to the physical parameters of the primary lens, namely, the Einstein timescale $t_{\rm E}$, the angular Einstein radius $\theta_{\rm E}$, and the Einstein ring radius projected onto the observer plane $\tilde{r}_{\rm E}$, only $t_{\rm E}$ is routinely measurable from the lensing light curve. These three observables are related to the underlying physical lens parameters of the primary mass M, relative lens-source parallax $\pi_{\rm rel} = (1\ {\rm AU})(D_{ol}^{-1} - D_{os}^{-1})$, and proper motion $\mu_{\rm rel}$ by

$$t_{\rm E} = \frac{\theta_{\rm E}}{\mu_{\rm rel}}, \quad \theta_{\rm E} = \sqrt{\frac{4GM\pi_{\rm rel}}{c^2\ {\rm AU}}}, \quad \tilde{r}_{\rm E} = \sqrt{\frac{4GM\ {\rm AU}}{c^2\pi_{\rm rel}}}. \quad (2)$$

For the unique determination of the planet mass, one must therefore measure the other two observables, $\theta_{\rm E}$ and $\tilde{r}_{\rm E}$. Once $\theta_{\rm E}$ and $\tilde{r}_{\rm E}$ are known, the primary lens mass is determined by

$$M = \left(\frac{c^2}{4G}\right)\tilde{r}_{\rm E}\theta_{\rm E}, \quad (3)$$

and thus the mass of the planet by $m_p = qM$. In the case of free-floating planets, or bound planets in which the primary is *not* detected, one must measure the analogous quantities $\theta_{{\rm E},p}$ and $\tilde{r}_{{\rm E},p}$ to infer $m_p = (c^2/4G)\tilde{r}_{{\rm E},p}\theta_{{\rm E},p}$.

There have been several methods proposed to determine the masses of planets detectable by future lensing experiments. Bennett & Rhie (2002) pointed out that for some detected events due to bound planets, the proposed space lensing mission would detect enough light from the host lens star to determine its spectral type and so infer the mass. However, no more than approximately one-third of lenses are bright enough to be so detected, and furthermore, the planet mass can only be inferred if the microlensing signature of the primary is also detected, so that the mass ratio q can be inferred, and then the planet mass via $m_p = qM$. Thus, this method cannot be used to infer the mass of very wide separation planets in which the magnification of the primary is negligible.

A more direct method of determining masses of bound planets in the lensing zone was proposed by Gould et al. (2003). They first demonstrated that the precision and sampling of the space observations will be sufficient to routinely detect one projection of the vector quantity[5] $\boldsymbol{\pi}_{\rm E}$ from the primary event. They then demonstrated that a second projection of $\boldsymbol{\pi}_{\rm E}$ could be measured by combining observations from a satellite in an L2 orbit with ground-based observations. For this setup, an Earth-satellite baseline of $d_{\rm sat} \sim 0.005$ AU is sufficient to routinely detect the difference in the peak time of the planetary perturbation as seen from the Earth and satellite for low-mass planets. The difference can then be combined with the known Earth-satellite projected separation to measure the second projection of $\boldsymbol{\pi}_{\rm E}$. The two projections of $\boldsymbol{\pi}_{\rm E}$ yield the magnitude of $\tilde{r}_{\rm E}$. Moreover, for terrestrial planets with mass ratio $q \sim 10^{-5}$, the Einstein ring radii $\theta_{{\rm E},p} = q^{1/2}\theta_{\rm E}$ is of order the angular source size θ_* of a typical (main sequence) source. Therefore, the magnification pattern arising from the planet typically has structure on the scale of the source size, which gives rise to finite-source deviations on the planetary perturbation. A global fit to the light curve including finite-source effects allows us to measure $\rho_* = \theta_*/\theta_{\rm E}$. The angular size θ_* can be determined from its dereddened color and magnitude using an empirically calibrated color–surface brightness relation. Thus, a measurement of ρ_* can be used to infer $\theta_{\rm E}$ and thus complete the primary mass measurement via equation (3), and therefore the planetary mass using the inferred mass ratio.

Han et al. (2004) demonstrated that the same observational setup discussed by Gould et al. (2003) to determine the mass of bound planets can also be used to determine the masses of free-floating planets. The principles are generally the same; however, the primary difference is that microlensing events due to free-floating planets are essentially single-lens events, and the small caustic residing at the center of the planet's Einstein ring that exists for bound planets is absent. The lack of structure induced by this caustic is beneficial because it allows one to unambiguously determine both components of the planetary projected Einstein ring radius $\pi_{{\rm E},p}$ from the planetary event itself. However, it also implies that the cross section for significant finite-source effects is much smaller than in the bound-planet case, for which the caustic structure is significantly extended. Essentially, it is only possible to detect finite-source effects and so measure $\theta_{{\rm E},p}$ for those events in which the impact parameter of the source is of order the angular size of the star, i.e., events in which the source star transits the planet. The angular radius θ_* of a typical main-sequence source star in units of the Einstein ring radius $\theta_{{\rm E},p}$ of a planet is

$$\rho_{*,p} \equiv \frac{\theta_*}{\theta_{{\rm E},p}} \sim 0.6\left(\frac{m_p}{1\ M_\oplus}\right)^{-1/2}, \quad (4)$$

where we have assumed $\theta_* \simeq 0.6\ \mu$as, which is typical for main-sequence sources in the bulge, and $\pi_{\rm rel} \simeq 42\ \mu$as (i.e., $D_{ol} = 6$ kpc and $D_{os} = 8$ kpc). The fraction of events that transit the source is $O(\rho_{*,p})$, and therefore mass measurements are only routine for planets with masses for which $\rho_{*,p} \gtrsim 1$, i.e., $m_p \lesssim 0.3\ M_\oplus$, and are less common for larger mass planets.

Microlensing events caused by wide-separation planets have a gross structure similar to that of events caused by free-floating planets, and thus the mass of the planet can be determined in a similar way. A wide-separation planetary event here means an event in which the source passes close to the planet

[5] The vector $\boldsymbol{\pi}_{\rm E} = 1\ {\rm AU}/\tilde{\boldsymbol{r}}_{\rm E}$ has the magnitude of $\tilde{r}_{\rm E}$ and the direction of the relative source-lens proper motion.

of a wide-separation planetary system. Because the star-planet separation is very wide (and in particular, much bigger than the Einstein ring of the primary), the source trajectory typically approaches only the planet (and not the host star lens); thus, the light curve of the event is approximated by that of a free-floating planetary event. For wide-separation planetary events, however, the primary (parent star) provides a shear at the location of the planet of $\gamma = s^{-2}$. This shear produces a caustic of angular width $\sim 4\gamma\theta_{\mathrm{E},p}$ near the location of the planet.[6] This caustic can cause anomalies near the peak of the light curves, provided that the source trajectory passes close to the caustic. Han & Kang (2003) pointed out that these anomalies can be used to distinguish events caused by bound planets from those caused by free-floating planets. In addition, this extended caustic structure increases the cross section for significant finite–source size effects, thereby increasing the fraction of events for which it is possible to measure $\theta_{\mathrm{E},p}$ (and thus the planet mass) relative to the unbound case. Since the source must pass within $O(\theta_{\mathrm{E},p})$ of the planet to be detected, the fraction of planetary events with detectable deviations due to the presence of the caustic is $\sim 4\gamma \sim 4s^{-2}$.

In this paper we present a comprehensive discussion of the ability of microlensing to detect and characterize wide-separation planets, consolidating and augmenting the studies of Gould et al. (2003), Han et al. (2004), and Han & Kang (2003). We consider the ability of microlensing to distinguish free-floating planets from bound planets, as well as to measure the mass and projected physical separation of wide-separation planets, as a function of these parameters. The paper is organized as follows: In § 2 we discuss the lensing characteristics of wide-separation planetary events. In § 3 we estimate the probability of measuring $\rho_{*,p}$ from future space observations of wide-separation planetary events by performing detailed simulations of these events and assessing the resulting uncertainties in $\rho_{*,p}$ and $\theta_{\mathrm{E},p}$. In § 4 we summarize the ability of microlensing to detect and characterize wide-separation planets, as well as discuss methods of distinguishing planetary lensing events caused by free-floating planets from those caused by wide-separation planets. We conclude in § 5.

Much of this paper is technical and not of interest to all readers. Those who only want to understand the potential of next-generation microlensing surveys to detect and characterize wide-separation planets should skim § 4, focusing on Figure 7, and then read § 5 for a summary.

Throughout this paper, we assume that the lens system (star, planet, or both) is located at $D_{ol} = 6$ kpc and that the source is a solar-type star with radius $R = 1\ R_\odot$ located at $D_{os} = 8$ kpc. Thus, $\theta_* = 0.58\ \mu$as and $\pi_{\mathrm{rel}} = 41.7\ \mu$as. The relative proper motion is assumed to be $\mu_{\mathrm{rel}} = 26.0$ km s^{-1} kpc^{-1}. These values are the typical (i.e., median) ones predicted by detailed models of the Galaxy (Han & Gould 1995, 2003). They yield, for a (star or planet) lens of mass M, an event timescale of $t_{\mathrm{E}} \simeq 38.8\ \mathrm{days}(M/1\ M_\odot)^{1/2}$, an angular Einstein ring radius of $\theta_{\mathrm{E}} \simeq 582\ \mu\mathrm{as}(M/1\ M_\odot)^{1/2}$, a projected Einstein ring radius of $\tilde{r}_{\mathrm{E}} \simeq 13.9\ \mathrm{AU}(M/1\ M_\odot)^{1/2}$, and a dimensionless source size of $\rho_* \simeq 10^{-3}(M/1\ M_\odot)^{1/2}$. When specified, we assume a primary mass of $M = 0.3\ M_\odot$.

[6] This is typically referred to as the "planetary caustic." The planet also induces a shear on the primary and thus creates an additional, smaller "central" caustic near the position of the primary. Here we are concerned with events that pass near the planet, and thus the central caustic is unimportant except for the very small fraction of events that happen to have trajectories nearly parallel to the planet-star axis and so pass close to both the primary and planet.

2. WIDE-SEPARATION PLANETARY EVENTS

Generally, one can write the mapping from the lens plane to the source plane of N point masses with no external shear or convergence as

$$\zeta = z - \sum_{j=1}^{N} \frac{m_j/M}{\bar{z} - \bar{z}_{L,j}} \tag{5}$$

(Witt 1990), where $\zeta = \xi + i\eta$, $z_{L,j} = x_{L,j} + iy_{L,j}$, and $z = x + iy$ denote the source, lens, and image positions, respectively, $\bar{z}$ denotes the complex conjugate of z, and m_j/M are the mass fractions of the individual lens components $\left(\sum_j m_j = M\right)$. Here all angles are normalized to the Einstein ring radius θ_{E} of the total mass of the system M. The lensing process conserves the source surface brightness, and thus, the magnifications A_i of the individual images i correspond to the ratios between the areas of the images and the source. For an infinitesimally small source element, this is

$$A_i = \left| \left(1 - \frac{\partial\zeta}{\partial\bar{z}} \frac{\overline{\partial\zeta}}{\partial\bar{z}} \right)^{-1} \right|. \tag{6}$$

The total magnification is just the sum over all images, $A = \sum_i A_i$.

For a single lens ($N = 1$), one can easily invert the lens equation to solve for image positions (x, y) and magnifications as a function of the source position (ξ, η). This yields the familiar result that there are two images for every source position $\zeta \neq 0$. These two images have angular separations $\theta \equiv |z - z_L|$ from the lens of $\theta_\pm = 0.5[u \pm (u^2 + 4)^{1/2}]$, where $u \equiv |\zeta - z_L|$. The images $\theta_+ > 1$ and $\theta_- < 1$ are often referred to as the major and minor images, respectively.

A planetary lens is described by the formalism of a binary ($N = 2$) lens. In this case, the lens equation cannot be inverted algebraically. However, it can be expressed as a fifth-order polynomial in z, and the image positions are then obtained by numerically solving the polynomial (Witt & Mao 1995). One important characteristic of binary lensing is the formation of caustics, which represent the set of source positions at which the magnification of a point source becomes infinite. The number and size of these caustics depends on the projected separation s and the mass ratio q.

One can think of a wide-separation planet with $s \gg 1$ and $q \ll 1$ as a perturbation to the major image produced by the primary. The location of the major image produced by the primary is $\theta_+ = 0.5[u + (u^2 + 4)^{1/2}]$, and therefore a planet separated by s from its parent star will produce a "planetary" caustic on the star-planet axis at an angular separation from its parent star of $\hat{s} = s - 1/s$ (see Fig. 1). In addition, there will be a second, smaller "central" caustic located near the star (Griest & Safizadeh 1998). By choosing the origin in the image plane as the position of the planet and the origin in the source plane as the point on the star-planet axis with an angular separation $\hat{s}$ from the primary and then normalizing all angles to the Einstein ring of the secondary, it is straightforward to show that, in the limit $s \gg 1$ and $q \ll 1$, the binary-lens equation becomes

$$\hat{\zeta} = \hat{z} - \frac{1}{\hat{\bar{z}}} + \gamma\hat{\bar{z}} \tag{7}$$

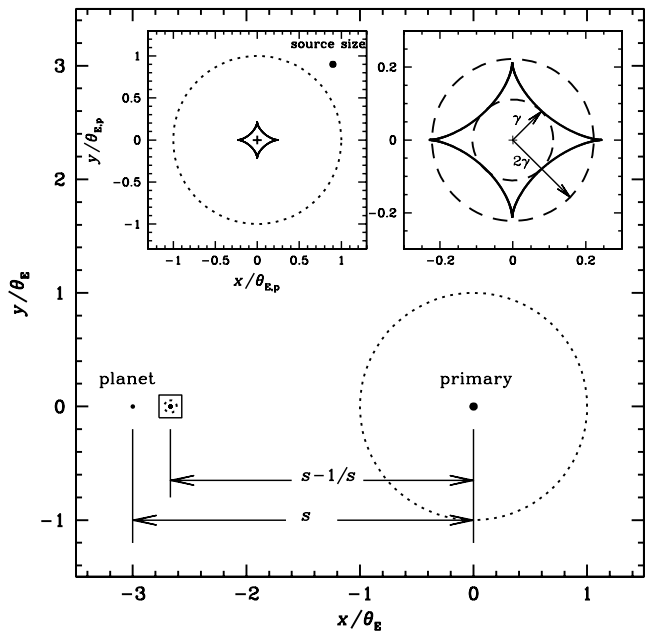

FIG. 1.—Lensing geometry of a star with a wide-separation planet. Shown are the locations of the star (at the origin), planet (at $[x, y] = [-3, 0]\theta_{\rm E}$), and the resulting caustics. The tiny central caustic is located very close to the star, and the planetary caustic is located in the region enclosed by the small square. The upper left inset is a blow-up of the region around the planetary caustic. The dotted circles represent the Einstein rings of the individual lens components around their effective lens positions. The upper right inset shows the planetary caustic enclosed by two circles with radii of 1.0γ and 2.0γ, respectively, where γ is the shear. The geometry is for the case in which the planet/star mass ratio is $q = 3\times10^{-3}$ and the normalized separation is $s = 3$. The small filled circle at the upper right corner of the left inset represents the size of a source star with a radius $R = 1.0\ R_\odot$ at $D_{os} = 8$ kpc. For the lens, we assume $M = 0.3\ M_\odot$ and $D_{ol} = 6$ kpc, and thus the angular Einstein radius is $\theta_{\rm E} = 0.32$ mas. Note that the axes of the main panel are scaled by the combined Einstein radius ($\theta_{\rm E}$), while the axes of the insets are scaled by the Einstein ring radius of the planet ($\theta_{{\rm E},p} = \sqrt{q}\theta_{\rm E}$).

(Dominik 1999). Here $\gamma = s^{-2}$ is the shear, and the notations with the hat represent length scales normalized by the Einstein radius corresponding to m_2, e.g., $\hat{z} = z(\theta_{\rm E}/\theta_{{\rm E},2})$. This is the well-known Chang & Refsdal (1979, 1984) lens. In its range of validity, equation (7) implies that if the planetary separation is sufficiently wide, the lensing behavior in the region around the planetary Einstein ring can be approximated as that of a single point-mass lens superposed on a uniform background shear γ. The caustics created by a Chang-Refsdal lens with $\gamma < 1$ have an asteroid shape (see Fig. 1) with a full width along the star-planet axis and a height normal to the planet-star axis of, respectively,

$$2a_{\rm C\text{-}R} = \frac{4\gamma}{\sqrt{1-\gamma}}, \qquad 2b_{\rm C\text{-}R} = \frac{4\gamma}{\sqrt{1+\gamma}}. \tag{8}$$

Thus, as the separation between the star and planet increases, the size of the caustic shrinks approximately as $1/s^2$, and both lens components tend to behave as if they are two independent single lenses.

For the applications discussed here, the angular size of the source is typically nonnegligible relative to the Einstein ring of the secondary, $\theta_{{\rm E},p}$. Therefore, finite-source effects must be taken into account. It is precisely these finite-source effects that allow one to measure $\theta_{{\rm E},p}$. The magnification of a finite source is computed by the intensity-weighted magnification averaged over the source star flux, i.e.,

$$A_{\rm fs}(\zeta) = \frac{\int_S I(\zeta')A(\zeta+\zeta')\,d\zeta'}{\int_s I(\zeta')\,d\zeta'}, \tag{9}$$

where A denotes the magnification of the corresponding point source, ζ is the vector position of the center of the source, ζ' is the displacement vector of a point on the source star surface with respect to the source star's center, and the two-dimensional integral is over the source-star surface S. For a source with uniform surface brightness, the computation can be reduced from a two-dimensional to a one-dimensional integral using the generalized Stokes's theorem (Gould & Gaucherel 1997; Dominik 1998). The finite-source effect becomes important when the source passes over a magnification pattern with small-scale structure or crosses the caustics. Because wide-separation planetary events have such extended magnification structures (i.e., the planetary caustics), the chance to measure $\rho_{*,p}$ is expected to be higher compared to the case of free-floating planet events.

In Figure 2 we show how the relative caustic and source sizes vary with respect to the Einstein radius for wide-separation planets with various mass ratios relative to and separations from the primary star, using the full binary lens formalism. For a fixed angular source size θ_*, the normalized source size $\rho_{*,p}$ becomes smaller with increasing planet/star mass ratio (as $\rho_{*,p} \propto q^{-1/2}$). However, in the parameter regimes shown in the figure, the Chang-Refsdal approximation is excellent, and therefore the size of the caustic in units of $\theta_{{\rm E},p}$ depends almost solely on s. Thus, as the separation increases, the caustic width decreases as $\sim 4\gamma \propto s^{-2}$.

3. PROBABILITY OF MEASURING $\theta_{{\rm E},p}$

We now address the question of what fraction of wide-separation planetary events in future lensing experiments will yield an accurate measurement of $\theta_{{\rm E},p}$. We estimate the probability P that a given wide-separation planetary event will exhibit substantial finite-source effects and so allow the measurement of $\rho_{*,p}$ to a given accuracy (in turn yielding $\theta_{{\rm E},p}$). In particular, we are interested in how the existence of the caustic created by the shear from the primary increases the probability relative to a free-floating planet event with similar lensing characteristics.

A wide-separation planetary lensing event can generally be described by nine parameters, namely, F_S, F_B, $t_{{\rm E},p}$, t_0, $u_{0,p}$, $\rho_{*,p}$, s, q, and α. We describe each of these in turn. The flux of the source F_S and the flux of any light blended with the source F_B are linearly related to the observed flux at time t by $F(t) = F_S A(t) + F_B$. The parameters $t_{{\rm E},p}$, t_0, and $u_{0,p}$ describe the trajectory of the source relative to the position of the planet in units of the planetary Einstein ring radius $\theta_{{\rm E},p}$. Here $t_{{\rm E},p}$ is the time required for the source to cross $\theta_{{\rm E},p}$, t_0 is the time of the closest approach to the planetary caustic, and $u_{0,p}$ is the separation (normalized by $\theta_{{\rm E},p}$) at that moment. These quantities are generally measurable from the gross features of the planetary events; in the simplest model, $u_{0,p}$ is related to the peak magnification, t_0 is when the event peaks, and $t_{{\rm E},p}$ is roughly the duration of the event. Next, $\rho_{*,p}$ is the source size in units of $\theta_{{\rm E},p}$. This parameter is typically derived from detailed modeling of the planetary event but is generally inferred from the magnitude and duration of the "smoothing" of the light curve due to the finite source size. Finally, s, q, and α are related to

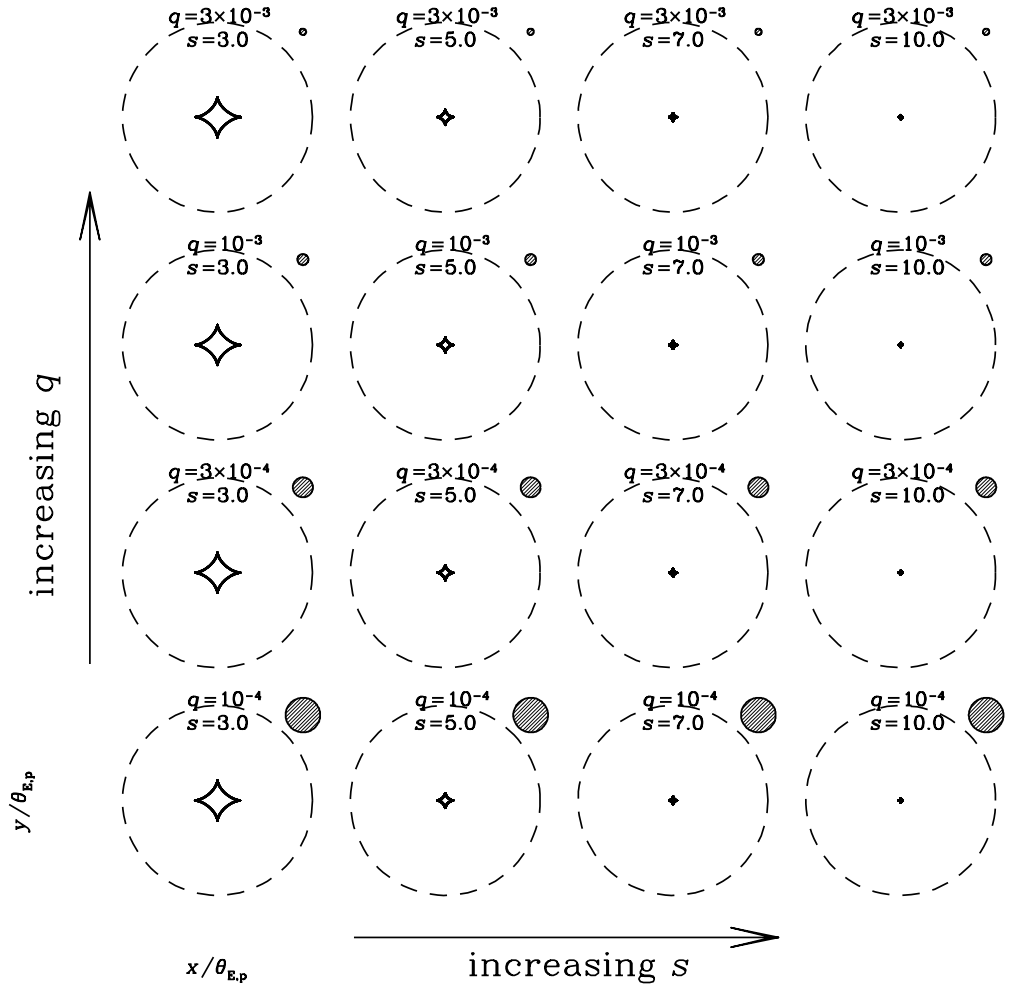

FIG. 2.—Variations of the caustic and source sizes relative to the size of the planetary Einstein ring of wide-separation planets with various mass ratios relative to and separations from the primary star. In each panel, the diamond-shaped figure is the planetary caustic, the dashed circle represents the Einstein ring of the planet, and the small filled circle in the upper right corner represents the size of the source star relative to the planetary Einstein ring. Panels are arranged so that the separation and mass ratio are increasing along the abscissa and ordinate, respectively. In the assumed geometry, the lens and source star are located at $D_{ol} = 6$ kpc and $D_{os} = 8$ kpc, respectively, and the source star has a physical radius of $R_* = 1.0\ R_\odot$. [*See the electronic edition of the Journal for a color version of this figure.*]

the star/planet system and are generally only well constrained if the microlensing signature of the primary is present. Here s is the separation of the planet from the primary in units of $\theta_{\rm E}$, q is the mass ratio of the system, and α is the orientation angle of the source trajectory with respect to the star-planet axis. Because the properties of wide-separation planetary events are primarily determined by the planet alone, and q is generally not well constrained, we adopt parameters normalized by the Einstein ring of the planet ($t_{{\rm E},p}$,$u_{0,p}$, and $\rho_{*,p}$) rather than their more poorly constrained analogs ($t_{\rm E} = q^{1/2} t_{{\rm E},p}$, $u_0 = q^{1/2} u_{0,p}$, and $\rho_* = q^{1/2}\rho_{*,p}$).

In order to estimate the probability P, we carry out detailed simulations of wide-separation planetary events and estimate the uncertainties of $\rho_{*,p}$ determined from simulated light curves. Although wide-separation planetary events are reasonably well described by the Chang-Refsdal approximation, in order to make our results fully general, we carry out our simulations using the full binary lens formalism. However, we use the Chang-Refsdal approximation to aid in the interpretation of our results. The simulations proceed as follows: Planetary microlensing event light curves are calculated using equations (5) and (6). The ranges of the planetary separations and mass ratios of the tested events are $2 \le s \le 20$ and $10^{-5} \le q \le 10^{-2}$, respectively. Finite-source effects are incorporated by computing a one-dimensional line integral along the boundaries of the images, whose positions are obtained by numerically solving the lens equation and then applying Stokes's theorem. The majority of target stars to be monitored by the proposed space microlensing mission are Galactic bulge main-sequence stars; we therefore assume a solar-type source star with an apparent magnitude of $I \sim 21$. For the space observations, we use specifications similar to the *MPF* mission (Bennett & Rhie 2002) and assume that events are monitored with a frequency of $f_{\rm obs} = 5\ {\rm hr}^{-1}$ and that a 600 s exposure image is acquired from each observation. We assume a photon acquisition rate of 13 photons s^{-1} for an $I = 22$ star.

In principle, one could determine the uncertainties of the fit parameters $p = (F_S,\ F_B,\ t_{{\rm E},p},\ t_0,\ u_{0,p},\ \rho_{*,p},\ s,\ q,\ \alpha)$ by generating many realizations of simulated light curves, including errors, fitting these light curves, and determining the variance in the fitted parameters. In practice, this approach is impractical and unnecessary. Rather, we estimate the expected uncertainty in the fit parameters by evaluating the curvature matrix of the χ^2 surface. Here the uncertainties of the

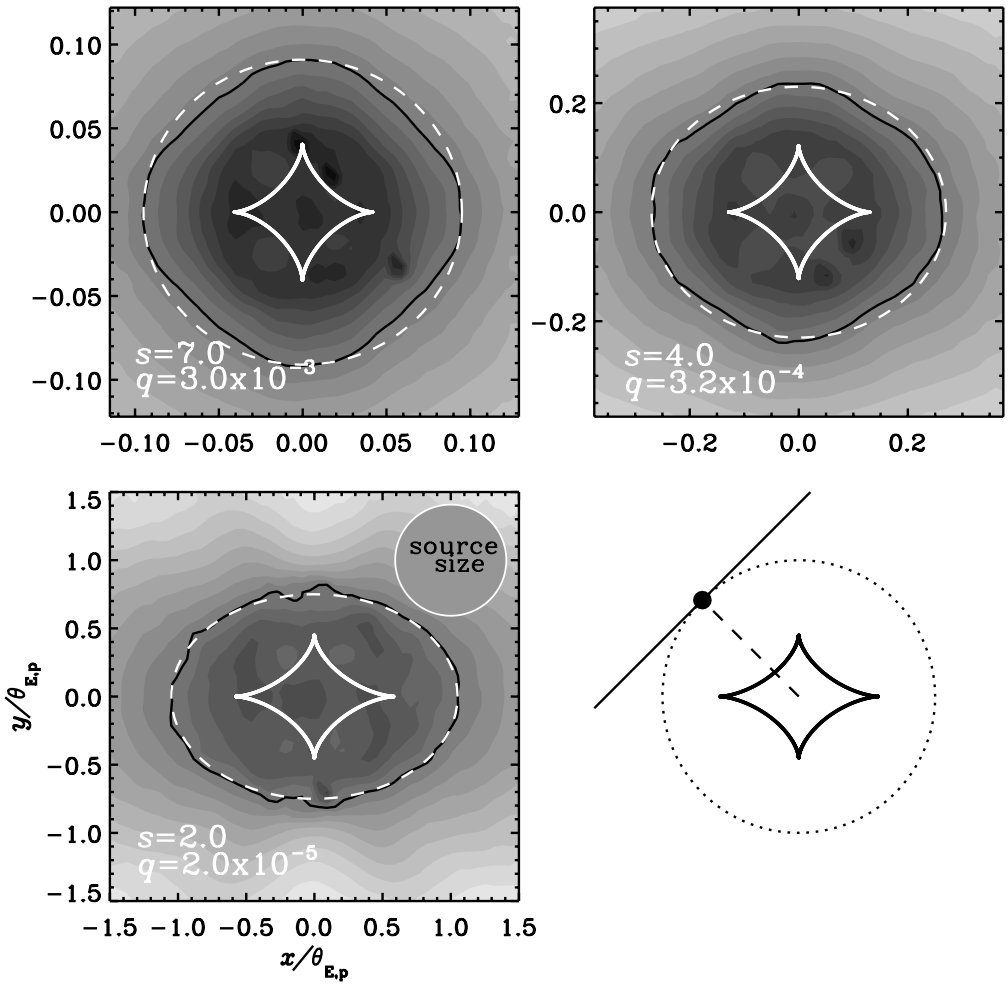

FIG. 3.—Contour maps of the fractional uncertainty $\sigma_{\rho_{*,p}}/\rho_{*,p}$ as a function of the source position relative to the planetary caustic. Each position on the map represents a source trajectory that passes through that position and is normal to the line connecting the position and the caustic center (see the geometry in the bottom right panel). For all three presented cases, the source size relative to the caustic size is nearly the same. The dark closed curve in each panel represents the contour at which $\sigma_{\rho_{*,p}}/\rho_{*,p} = 10\%$, and the white dashed curve shows the approximation of this contour as an ellipse.

individual fitting parameters (p_i) are determined from each light curve by

$$\sigma_i = \sqrt{c_{ii}}, \quad c = b^{-1}, \tag{10}$$

where c_{ij} is the covariance matrix and the curvature matrix of the χ^2 surface is defined by

$$b_{ij} = \sum_{k=1}^{N_{\rm obs}} \frac{\partial F_k}{\partial p_i}\frac{\partial F_k}{\partial p_j}\frac{1}{\sigma_k^2}. \tag{11}$$

Here $F_k(t) = A(t_k)F_S + F_B$ represents the observed flux for each measurement at time t_k, $N_{\rm obs}$ is the total number of measurements, and σ_k is the measurement error.

According to the luminosity function of the Galactic bulge field (Holtzman et al. 1998), the surface number density of stars with $I \lesssim 24$ is $\sim$5000 stars arcmin^{-2} $\sim$1.4 stars arcsec^{-2}, and thus a space mission equipped with an $\sim$1 m telescope can resolve most neighboring stars. However, since one cannot exclude the possibility of blending with light from a companion to the source or with the lens itself, we include the blending parameter F_B. For the simulation, we set the blending fraction to be $F_B/F_S = 0.3$. The photometric uncertainty is assumed to be limited by photon statistics, and the uncertainties of the fitting parameters are determined from the light curve measured during $-2.0t_{{\rm E},p} \le t - t_0 \le 2.0t_{{\rm E},p}$.

As we argued in § 2, the lensing behavior of a wide-separation planet is locally well described by a single lens with external shear $\gamma = s^{-2}$, i.e., a Chang-Refsdal lens. Therefore, the magnification structure can be described by only two parameters, namely, γ and $\rho_{*,p}$, rather than the three parameters s, q, and ρ_* generally required for full binary lensing. In fact, for $\gamma \ll 1$ ($s \gg 1$), the Chang-Refsdal lens becomes self-similar: when all angles are normalized to 2γ, the magnification pattern is nearly independent of γ. Therefore, the ability to measure $\rho_{*,p}$ depends primarily on the single parameter $\rho_{*,p}/\gamma$. In fact, this scaling breaks down for two reasons. First, as γ approaches unity, the self-similarity of the Chang-Refsdal lens breaks down. Second, because we are considering a fixed sampling rate, the number of samples per planetary crossing time $t_{{\rm E},p} = q^{1/2}t_{\rm E}$ decreases for smaller mass planets. Therefore, the error on the light-curve fit parameters, which depends on both the magnification structure and the density of data points, formally depends on q as well. However, these two effects are generally subdominant, and therefore the dependence on γ or q for fixed $\rho_{*,p}/\gamma$ is relatively weak. We demonstrate this by computing the fractional uncertainty $\sigma_{\rho_{*,p}}/\rho_{*,p}$ as a function of the source positions around the planetary caustic. Figure 3 shows the

contour maps of $\sigma_{\rho_{*,p}}/\rho_{*,p}$ for three different combinations of s and q, yielding the same ratio of $\gamma/\rho_{*,p}$. In the maps, each position represents a source trajectory that passes through that position and is normal to the line connecting the position and the caustic center (see the geometry illustrated in the bottom right panel), and the closed curve drawn by a dark line represents the contour at which $\sigma_{\rho_{*,p}}/\rho_{*,p} = 10\%$. From a comparison of the maps, one finds that the patterns look qualitatively similar despite the great differences in the values of s and q, confirming the argument that the ability to measure $\rho_{*,p}$ depends primarily on $\rho_{*,p}/\gamma$.

A straightforward approach to estimating P would be first to construct maps of $\sigma_{\rho_{*,p}}/\rho_{*,p}$ such as the ones shown in Figure 3 for the various combinations of s and q, second to draw many light curves with various combinations of $u_{0,p}$ and α obtained from one-dimensional cuts through each constructed map, and then to estimate the probability as the ratio between the number of light curves yielding uncertainties smaller than a threshold value out of the total number of tested events. However, we find that this approach is difficult to implement because constructing the large number of high-resolution maps that incorporate finite-source effects demands a large amount of computation time even after the great reduction of finite-source calculations using Stokes's theorem (i.e., from a two-dimensional to a one-dimensional integral). Fortunately, we find that the region where $\rho_{*,p}$ can be measured to a given precision (the effective region) is well confined around the planetary caustic, and its boundary is, in general, approximated as an ellipse, as illustrated in Figure 3. We therefore estimate P by determining the semimajor axis a and semiminor axis b of the ellipse and then compute the probability, which corresponds to the ratio of the angle-averaged cross section of the ellipse to the diameter of the planetary Einstein ring (see Fig. 4),[7] by

$$P = \frac{1}{\pi}\int_0^{\pi} \sqrt{a^2 \sin^2\alpha + b^2 \cos^2\alpha}\, d\alpha = \frac{2}{\pi} aE(e), \qquad (12)$$

where E represents the complete elliptical integral of the second kind and $e = (1 - b^2/a^2)^{1/2}$. Note that, since a and b are in units of $\theta_{\mathrm{E},p}$, the probability is normalized such that P is the fraction of events with $u_{0,p} \leq 1$ that yield a measurement of $\rho_{*,p}$ to a given factional precision $\sigma_{\rho_{*,p}}/\rho_{*,p}$. Planetary events with $u_{0,p} > 1$ may well be detectable in the next-generation lensing surveys, and thus the fraction of detectable planetary lensing events with a measurement of $\rho_{*,p}$ to a given accuracy is likely to be smaller. We address this point in § 4.

Figure 5 shows the contour map (marked by white contours and gray scale) of the determined probability P as a function of the planetary separation and mass ratio. For the map, the imposed threshold uncertainty is $(\sigma_{\rho_{*,p}}/\rho_{*,p})_{\mathrm{th}} = 10\%$. From the

[7] The approximation of the boundary of the effective region as an ellipse becomes poor as the source size becomes smaller than the caustic size. In the limiting case $\rho_{*,p} \ll \gamma$, the positions at which finite-source effects are large (allowing $\rho_{*,p}$ to be effectively measured) are confined to regions near the caustic itself, as well as the protruding region outside the caustic cusps (Fig. 4, *dark-shaded regions*). Even in this limiting case, however, we note that the probability P determined by eq. (12) is still a good approximation. This is demonstrated in Fig. 4, in which the light-shaded region enclosed by the clover-shaped figure represents the effective region of source trajectories that can pass the dark-shaded region, and the dashed circle represents the boundary of the effective region following the ellipse approximation. We find that even in this extreme case, the ratio between the angle-averaged cross sections of the clover-shaped and circular regions is 0.903, implying that the error in the probability as determined by the ellipse approximation is not important.

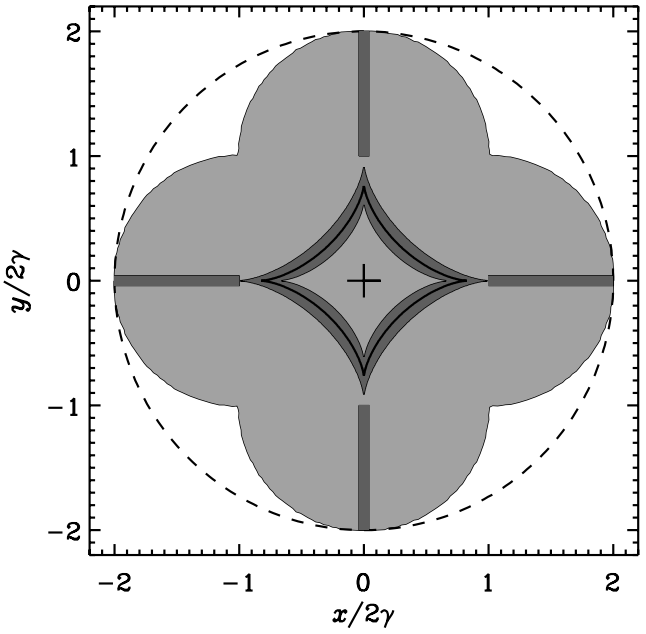

FIG. 4.—Cartoon showing the validity of approximating the effective region for $\rho_{*,p}$ measurement as an ellipse. Here the dark-shaded area represents the source positions where, for $\rho_{*,p} \ll \gamma$, finite-source effects are large, thus allowing $\rho_{*,p}$ to be effectively measured. The light-shaded region enclosed by the clover-shaped figure represents the effective region of source trajectories that pass the dark-shaded region, and the dashed circle represents the boundary of the effective region following the ellipse approximation. We note that the cross sections of the dark- and light-shaded regions are, by definition, the same. All lengths are normalized by the caustic size, i.e., 2γ.

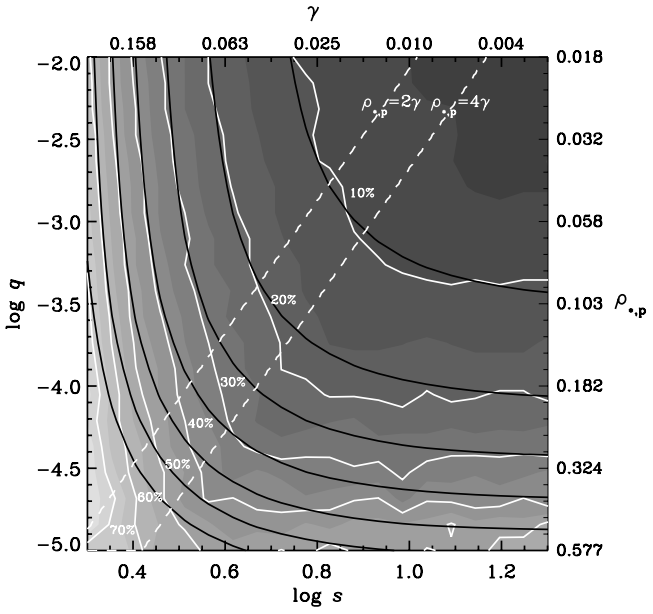

FIG. 5.—Probability P of measuring $\rho_{*,p}$ for wide-separation planetary events as a function of the planetary separation and mass ratio. The adopted threshold uncertainty is $(\sigma_{\rho_{*,p}}/\rho_{*,p})_{\mathrm{th}} = 10\%$. The two sets of contours drawn by dark and white lines are based on numerical computations considering full binary lensing and an analytic treatment using Chang-Refsdal lensing, respectively (see the text for details). The gray-scale tones show the probability P based on numerical computations: they change for every 5% change of P. The two dashed straight lines represent the positions at which $\rho_{*,p} = 2.0\gamma$ and 4.0γ, respectively.

probability map, we find two basic regimes. First, in the region of parameter space where the caustic size is much smaller than the source size, the contribution of the caustic to the probability is not important, and the value of P is essentially the same as that for the corresponding free-floating events. Since $\rho_{*,p}$, which is the dominant factor determining P in this region, depends only on the mass ratio and does not depend on the separation, the probability distribution is flat, as shown in the lower right part of Figure 5. On the other hand, in the region where the caustic size is of order or larger than the source size, the contribution of the caustic to P becomes important. The caustic size, and thus P, rapidly increase with the decrease of the planetary separation, and this is reflected in the probability distribution trends in the upper left part of Figure 5. We find that the two regions (i.e., source- and caustic-size–dominant regions) are divided roughly by the line $\rho_{*,p} = 4\gamma$. Knowing that the relative cross section for $\rho_{*,p}$ measurement results from the combination of the caustic and normalized source sizes and keeping the validity of the Chang-Refsdal lensing in mind, we interpret the result by analytically assessing the probability based on the semimajor and semiminor axes of the effective region as the linear combination of the Chang-Refsdal caustic size and the normalized source radius, i.e.,

$$a = \mathcal{C}_\gamma a_{\text{C-R}} + \mathcal{C}_{\rho_*}\rho_{*,p},$$
$$b = \mathcal{C}_\gamma b_{\text{C-R}} + \mathcal{C}_{\rho_*}\rho_{*,p}, \qquad (13)$$

where $a_{\text{C-R}}$ and $b_{\text{C-R}}$ are defined in equation (8) and $\mathcal{C}_\gamma$ and $\mathcal{C}_{\rho_*}$ are linear coefficients. In the point-mass limit ($\gamma \ll \rho_{*,p}$), it is known that $\rho_{*,p}$ can be measured only when the lens crosses the source star (Gould & Welch 1996), and thus we set $\mathcal{C}_{\rho_*} = 1.0$. By adjusting $\mathcal{C}_\gamma$, we find that $\mathcal{C}_\gamma \sim 2.5$ yields the best-fit probability distribution (Fig. 5, *dark contours*) to the one based on numerical computations. This implies that in the caustic-dominant regime, the effective cross section of the caustic for a $\rho_{*,p}$ measurement is larger than its full width by $\sim$25%, i.e., $a/(4\gamma) \simeq 1.25$.

In our simulations, we assumed a primary of mass $M = 0.3\ M_\odot$, and thus one might suspect that our results are only valid for this specific choice of primary mass. However, since the errors in the fit parameters are primarily determined by the timescale of the planetary perturbation $t_{\text{E},p}$ and the planetary Einstein ring radius $\theta_{\text{E},p}$, and thus the mass of the planet m_p, changing the primary mass will have essentially no effect on the resulting errors in $\rho_{*,p}$, provided that q is also changed so that the mass of the planet $m_p = qM$ is fixed. Thus, changing the primary mass effectively amounts to a rescaling of the ordinate in Figure 5.

Translating a measurement of $\rho_{*,p}$ into a measurement of $\theta_{\text{E},p}$ requires knowledge of the angular size of the source θ_*. This can be estimated from the known source color and magnitude, as described in Yoo et al. (2004a). Briefly, the process works as follows: The apparent source color and apparent magnitude can be estimated from multicolor photometry taken at several different source magnifications. The dereddenned color and magnitude can then be found by comparing with the apparent color and magnitude of nearby stars in the red clump, whose dereddened color and magnitude are known. This assumes that the source star is being seen through the same column of dust as the stars in the red clump. In practice, however, even fairly large differences in the dust column have relatively little effect because the source color and magnitude have opposite effects on the inferred value of θ_*. The angular size θ_* of the source can then be inferred from its color and magnitude using an empirical color–surface brightness relation (e.g., van Belle 1999). The statistical error in the derived value of θ_* from this procedure will likely be dominated by the intrinsic scatter in the empirical color–surface brightness relation, which is currently $\sim$10%. Therefore, the error in the inferred value of $\theta_{\text{E},p}$ will be dominated by the error in $\rho_{*,p}$ for $\sigma_{\rho_{*,p}}/\rho_{*,p} \gtrsim 10\%$.

4. DETECTION AND CHARACTERIZATION OF WIDE-SEPARATION PLANETS

In this section we summarize the potential of next-generation microlensing surveys to characterize wide-separation planets, focusing on their ability to distinguish isolated planetary events caused by free-floating planets from those caused by wide-separation planets as a function of the separation of the planets from their host stars. As the formation processes and evolution histories of wide-separation and free-floating planets are believed to be substantially different, unless these two populations of planetary events can be distinguished, it will be difficult to extract useful information about the formation and evolution of these individual planet populations.[8] We also summarize the capacity of these surveys to measure the masses of the planets through the measurement of $\theta_{\text{E},p}$ and $\tilde{r}_{\text{E},p}$ as a function of the planet mass and separation. The majority of the calculations in the following sections are independent of the mass of the primary, and so our results are most naturally expressed in terms of their dependence on the planet mass m_p rather than the planet mass ratio q. However, to make contact with the results from the previous sections, we also quote results in terms of q, assuming a primary mass of $M = 0.3\ M_\odot$, i.e., $q = 10^{-5}(m_p/1\ M_\oplus)$.

4.1. *Cross Section for Detection*

We first address the question of the detectability of planets as a function of their mass. For fixed μ_{rel} and π_{rel} and for identical observational setups, larger mass planets are detectable to larger planetary impact parameters $u_{0,p}$ because the number of points per crossing time is larger, thereby increasing the signal-to-noise ratio (S/N). This implies a larger cross section for detection. As the mass ratio decreases, the minimum impact parameter required to produce a light curve above a given S/N decreases, thus decreasing the cross section for detection. Eventually, finite–source size effects become important when $\rho_{*,p} \gtrsim 1$. For sufficiently high photometric accuracy, finite-source effects can increase the cross section, since the timescale for the event will be set by the crossing time of the source, $t_* \equiv \theta_*/\mu_{\text{rel}}$, rather than the planetary Einstein crossing time, $t_{\text{E},p}$. Eventually, however, when $\rho_{*,p} \gg 1$ the deviation due to the planet will be completely suppressed, and the planet will be undetectable. To quantify these trends, we determine the expected S/N of an isolated single-lens event,

$$\text{S/N} = \frac{N^{1/2}}{\sigma}\left\{\int d\tau \left[1 - A_{\text{fs}}\left(\tau;\ u_{0,p},\ \rho_{*,p}\right)^{-1}\right]^2\right\}^{1/2}, \qquad (14)$$

[8] In fact, the frequency of bound and free-floating planets must be determined statistically from the ensemble of observed planetary events. As we demonstrate in § 4.3, the majority of events from wide planets with $r_\perp \gtrsim 20$ AU will show no signature of the primary, and so it is not generally possible to distinguish between bound and free-floating planets on an event-by-event basis. Therefore, it will be necessary to use those events that are known to be due to bound planets to statistically infer the fraction of events with no signature of a primary that are due to bound planets.

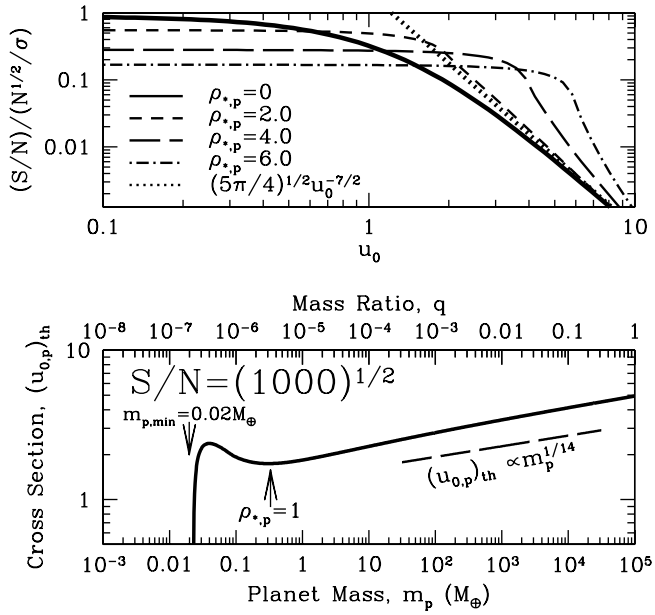

FIG. 6.—*Top*: (S/N)/($N^{1/2}/\sigma$) as a function of the impact parameter u_0, for single-lens events with various values of the source size $\rho_{*,p}$ in units of the Einstein ring radius. Here N is the number of points per Einstein crossing time, each with fractional precision σ. The solid curve is for a point source ($\rho_{*,p} = 0$), and the dotted curve shows the limiting form for a point source light curve with $u_0 \gg 1$, i.e., eq. (15). *Bottom*: Cross section $(u_{0,p})_{\rm th}$ to detect a planet at $S/N \geq (1000)^{1/2}$ (*solid curve*) as a function of its mass m_p (*bottom axis*) and mass ratio q (*top axis*). The long-dashed line shows the scaling $(u_{0,p})_{\rm th} \propto m_p^{1/14}$, which is valid for point sources and $(u_{0,p})_{\rm th} \gg 1$. Also shown are the minimum detectable planet mass, $m_{p,\rm min} \simeq 0.02\ M_\oplus$, and the mass at which $\rho_{*,p} = 1$.

where N is the number of measurements per planet Einstein crossing time $t_{{\rm E},p}$, σ is the fractional precision of each measurement, $A_{\rm fs}$ is the finite-source magnification, and $\tau \equiv (t - t_0)/t_{{\rm E},p}$ is the time from the peak of the planetary event in units of the Einstein crossing time. Although we assume the magnification is described by single-lens event with no external shear, our results are approximately applicable to wide-separation planets as well. This is because, as we demonstrate below, planets with mass $m_p \gg 1\ M_\oplus$ are detectable with impact parameters $u_{0,p} \geq 1$, where any deviation arising from the caustic induced by the primary will be negligible. On the other hand, for low-mass planets with $\rho_{*,p} \geq 1$, the deviation due to the caustic vanishes up to fourth order in $\rho_{*,p}^{-1}$ when the source completely encloses the caustic (Gould & Gaucherel 1997). Therefore, the isolated point-lens approximation should be sufficient except for a relatively small range near $m_p \sim 0.3\ M_\oplus$, where we generally underestimate the S/N.

Figure 6 (*top*) shows the normalized signal-to-noise ratio, (S/N)/($N^{1/2}/\sigma$), as a function of the impact parameter u_0 for source sizes $\rho_{*,p} = 0.0$, 2.0, 4.0, and 6.0. For small sources, $\rho_{*,p} \ll 1$, and high-magnification events, $u_{0,p} \ll 1$, the term in braces in equation (14) is approximately unity and independent of $u_{0,p}$, and so $S/N \sim N^{1/2}\sigma^{-1}$. In the opposite limit of large impact parameter events, $u_{0,p} \gg 1$, we find

$$S/N = \sqrt{\frac{5\pi N}{4}}\sigma^{-1}u_{0,p}^{-7/2}. \tag{15}$$

Figure 6 (*bottom*) shows the impact parameter $(u_{0,p})_{\rm th}$ for which the S/N is equal to the threshold value $(S/N)_{\rm th} = (1000)^{1/2}$, for the same assumptions adopted in the simulations described in § 3, namely, $f_{\rm obs} = 120\ {\rm day}^{-1}$ and $\sigma = 1\%$. This is the appropriate threshold for detecting isolated events in otherwise constant stars (Bennett & Rhie 2002). This critical impact parameter $(u_{0,p})_{\rm th}$ corresponds to the cross section for the detection of a planet of mass m_p. In the small-source, large–impact parameter limit, this can be written as

$$(u_{0,p})_{\rm th} \sim 2.3\left(\frac{m_p}{1\ M_\oplus}\right)^{1/14}\left(\frac{f_{\rm obs}}{120/1\ {\rm day}}\right)^{1/7} \times \left(\frac{\sigma}{0.01}\right)^{-2/7}\left[\frac{(S/N)_{\rm th}}{\sqrt{10^3}}\right]^{-2/7}, \tag{16}$$

where $f_{\rm obs}$ is the observational frequency. Therefore, large mass ratio planetary events can generally be detected with planetary impact parameters significantly larger than unity.

In the limit of large sources, $\rho_{*,p} \gg 1$, the magnification is strongly affected by finite-source effects. In this case, the light curve is reasonably well approximated as a boxcar with a duration of $\sim 2t_*$ and an amplitude $A_{\rm fs} \sim 1 + 2\rho_{*,p}^{-2}$ (Di Stefano & Scalzo 1999a; Agol 2003), implying an S/N of

$$S/N \sim \frac{N^{1/2}}{\sigma}\frac{2^{3/2}\rho_{*,p}^{1/2}}{2 + \rho_{*,p}^2}. \tag{17}$$

Therefore, for a fixed θ_* and $\mu_{\rm rel}$, planets with a mass less than

$$m_{p,\rm min} \sim 0.02\ M_\oplus\left(\frac{f_{\rm obs}}{120/1\ {\rm day}}\right)^{-1/2}\frac{\sigma}{0.01}\frac{(S/N)_{\rm th}}{\sqrt{10^3}} \tag{18}$$

cannot be detected because of finite-source effects. This limit is shown in Figure 6 (*bottom*) and corresponds to roughly a lunar mass, or a mass ratio of $q \sim 2 \times 10^{-7}$ for a primary mass of $\sim 0.3\ M_\odot$. Planets with mass ratio larger than this limit but still well into the finite-source–dominated regime will have a detection cross section of $(u_{0,p})_{\rm th} \sim \rho_{*,p}$, which is generally larger than the corresponding point-source cross section. Therefore, for the parameters we have adopted, the cross section as a function of decreasing q first decreases until $\rho_{*,p} \sim 1$ and then increases until $m_{p,\rm min}$, at which point it suddenly plummets (see Fig. 6).

4.2. *Mass Measurement*

We now estimate the fraction of *detectable* events that yield accurate mass measurements, incorporating our estimate for the cross section for detection from § 4.1. In Figure 7 we plot the boundary of the region in the (m_p, $r_\perp$) or (q, s) plane where more than 50% of detectable wide-planet events yield a 10% measurement of $\rho_{*,p}$ (*thick solid curve*). Here we adopt the analytic form for the cross section of measuring $\rho_{*,p}$ to 10% given in equation (13) with $\mathcal{C}_\gamma = 2.5$ but normalize to the number of detectable events by dividing the resulting probability by $(u_{0,p})_{\rm th}$. We also show in Figure 7 an approximation to the boundary of the region in the (m_p, $r_\perp$) or (q, s) plane at which we expect $\sim$50% of detectable events to yield a 10% measurement of $\tilde{r}_{{\rm E},p}$ from parallax effects arising from the difference in the light curve as seen from a satellite at L2 and a ground-based observer (*thick long-dashed curve*). Here we have assumed that a planet event detected at a given S/N yields a fractional error in the projected Einstein ring radius (Gould et al. 2003; Han et al. 2004) of

$$\frac{\sigma_{\tilde{r}_{\rm E}}}{\tilde{r}_{\rm E}} \sim \frac{\tilde{r}_{{\rm E},p}}{d_{\rm sat}}(S/N)^{-1}, \tag{19}$$

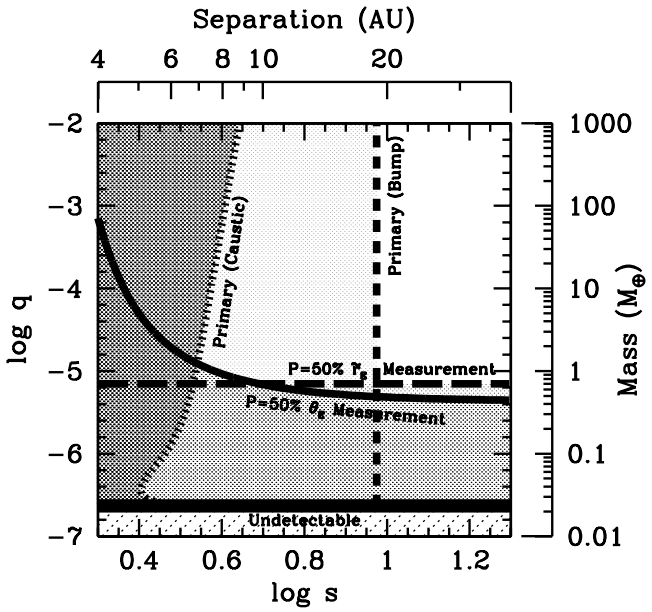

FIG. 7.—Characterization of wide-separation planets as a function of the planetary separation s and mass ratio q using a next-generation microlensing planet search. The heavy horizontal line shows the lower limit on the mass of detectable planets of $m_p \gtrsim 0.02\ M_\oplus$, or $q \gtrsim 2\times10^{-7}$. In this figure, planets are considered detected if they produce deviations with $S/N > (S/N)_{th} = (1000)^{1/2}$. The solid contour shows the upper boundary to the region in which more than 50% of detectable planetary events will yield a ~10% measurement of θ_E. Similarly, the long-dashed line shows the upper boundary to the region for which more than 50% of detectable planetary events will yield a ~10% measurement of $\tilde{r}_E$. The dotted contour shows the rightmost boundary of the region in which more than 50% of detectable planets can be identified as bound from the deviation caused by the planetary caustic from the nominal point-lens form, where $S/N > (160)^{1/2}$ is required for detection of the deviation. Similarly, the dashed vertical line shows the rightmost boundary of the region in which the magnification of the primary is detectable for more than 50% of events with $S/N > (160)^{1/2}$. The top and right axes show the conversion from (q, s) to $(m_p, r_\perp)$ assuming a primary mass of $M = 0.3\ M_\odot$ and $r_E = 2$ AU.

where $d_{sat} \sim 0.005$ is the projected Earth-satellite separation and we have assumed our fiducial value of $\pi_{rel} \simeq 42\ \mu$as, so that $\tilde{r}_{E,p} = 0.024\ \mathrm{AU}(m_p/1\ M_\oplus)^{1/2}$. We have ignored the effect of finite sources on the ability to measure $\tilde{r}_{E,p}$. We note that the approximation in equation (19) for the fractional error in $\tilde{r}_{E,p}$ is very crude; however, it captures the primary dependence on m_p and agrees reasonably well with more detailed calculations (Han et al. 2004).

Inspection of Figure 7 indicates that, by combining ground-based observations with those of a satellite in an L2 orbit, it should be possible to measure the mass of a majority of planetary events arising from planets with $m_p \lesssim 1\ M_\oplus$, corresponding to $q \lesssim 10^{-5}$, to a fractional precision of ~10%. Mass measurements will be possible for a smaller fraction of higher mass planets. However, since the overall detection rate for such planets will likely be higher, a similar or higher number of reasonably precise mass measurements may be possible.

4.3. *Detection of the Primary*

We now consider several methods by which the presence of the primary star can be detected in isolated events caused by wide-separation planets, thus permitting discrimination between bound and isolated planets. First, as discussed in detail by Han & Kang (2003), it will be possible to identify wide-separation planetary events from the signature of the planetary caustic near the peak of the light curves. Han & Kang (2003) found that signatures with ≥5% deviation can be detected for ≳80% of events with $u_{0,p} \leq 1$ caused by Jupiter-mass planets with separations ≲10 AU, and the probability is still substantial for separations up to even ~20 AU. Here we consider a simplified model for the probability of detecting the primary via the signature of the planetary caustic. We assume that the wide separation can be approximated by a Chang-Refsdal lens. We calculate the fractional deviation δ of the Chang-Refsdal lens from a single lens as a function of position along the two axes of symmetry. We assume that a light curve with a peak deviation δ can be distinguished from the single-lens case with

$$S/N \sim \frac{N^{1/2}}{\sigma}(4\gamma)^{1/2}\delta. \tag{20}$$

We then determine the semimajor and semiminor axes of the region around the planetary caustic at which the S/N is greater than a given threshold $(S/N)_{th}$. The fraction of detectable planetary events for which the primary can be detected via the deviation from a point lens is then given by equation (12) normalized by the cross section for detection, $u_{0,th}$. We choose $(S/N)_{th} = (160)^{1/2}$. This threshold is lower than that assumed for detection of the planetary event because there are fewer light curves to search for the deviation arising from the caustic. Figure 7 shows the region in the (q, s) plane where more than 50% of isolated events arising from bound planets give rise to detectable deviations due to the presence of the planetary caustic (*thick dotted line*). Our results agree well with the results of Han & Kang (2003), when the latter are normalized by $(u_{0,p})_{th}$.

Second, wide-separation planetary events can be distinguished by the additional long-term bumps in the light curve caused by the primary star. Compared to the planetary Einstein ring, the Einstein ring of the primary star is much larger, implying a larger effective lensing region. Combined with high-precision photometry from space observations, then, the existence of the primary star can often be noticed even without the signatures of the planetary caustic. In the limit of large impact parameter u_0, the bump due to the primary can be detected with the S/N given by equation (15). Then, the cross section to detect the primary-induced bump for a given $(S/N)_{th}$ is

$$P = \begin{cases} 1.0, & u_{0,\mathrm{th}} > s, \\ \dfrac{2}{\pi}\sin^{-1}\left(\dfrac{u_{0,\mathrm{th}}}{\hat{s}}\right), & u_{0,\mathrm{th}} < s, \end{cases} \tag{21}$$

where $u_{0,th}$ is given by equation (16) with $m_p \rightarrow M$. Figure 7 shows the contour (*thick short-dashed line*) at which $P = 50\%$ as a function of (s, q), assuming $(S/N)_{th} = (160)^{1/2}$ and $M = 0.3\ M_\odot$. We find that $P = 50\%$ for $s \simeq 9.2$, corresponding to $r_\perp \simeq 18$ AU. It will be possible to detect the primary for essentially all planets with $s \lesssim 6.52$, or $r_\perp \lesssim 13$ AU.

The third method of identifying a wide-separation planet is detecting blended light from the host star. According to Bennett & Rhie (2002), for approximately one-third of events with detected planets from a space lensing mission, the planetary host star is either brighter than or within ~2 mag of the source star's brightness.

When we consider the three methods discussed here together, the prospects for distinguishing isolated planetary events caused by bound and free-floating planets seem good. For roughly one-third of all events, regardless of the mass or separation of the planet, the flux from the primary should be detectable. For more than half of all events caused by wide-separation planets with $r_\perp \lesssim 5-9$ AU (depending on mass), the

influence of the primary will be detectable in the light curve via the planetary caustic. Finally, more than half of all detectable planets with $r_\perp \gtrsim 20$ AU can be inferred to be bound via the low-amplitude bump caused by the magnification of the primary.

5. CONCLUSION

With their excellent photometric precision and extremely high temporal sampling, next-generation microlensing planet searches will be sensitive to planets with masses almost as low as that of the Moon. These searches will employ large-format cameras with large fields of view in order to monitor hundreds of millions of stars simultaneously with ~10–20 minute sampling. Because all stars will be monitored continuously regardless of whether they are being lensed or not, such searches will be sensitive to isolated events caused by wide-separation or free-floating planets, in contrast to current microlensing planet searches. Such planets are very difficult or impossible to probe by other planet detection methods.

The scientific return of these wide-separation and free-floating planet detections would be greatly enhanced if their nature could be characterized. In particular, differentiating between wide-separation planets and free-floating objects is highly desirable, as is the measurement of their mass. Generally, the light curves of free-floating planets are grossly similar to those of wide-separation planets. Furthermore, microlensing light curves generally only yield event timescales, which are degenerate combinations of the mass, distance, and transverse velocity of the lens. However, as recently pointed out by several authors (Gould et al. 2003; Han & Kang 2003; Han et al. 2004), there are several unique properties of next-generation microlensing surveys that should allow better characterization of wide-separation and free-floating planets. Here we have summarized and built on previous works, addressing the ability of these searches to distinguish wide-separation planets from free-floating planets, as well as to measure planet masses.

We have performed detailed simulations of wide-separation planetary events and evaluated the probability of measuring the Einstein ring radius θ_E for these events; this is one of the two additional quantities needed to measure the lens mass. From this investigation, we find that the parameter space of the probability distribution is divided into two regimes depending on the ratio between the caustic and normalized source sizes. In the regime in which the source size is much larger than the size of the caustic, the probability is not much different from that of the corresponding free-floating planetary events. In the opposite regime in which the caustic size is much larger than the source size, the probability is significantly higher than the case without the caustic. As a result, the probability of θ_E determination for wide-separation planetary events can be substantially higher than that of free-floating planetary events. We find that the effective cross section of the caustic is about 1.25 times its linear size for small sources.

For the majority of events due to planets with mass $m_p \leq 1\ M_\oplus$, it should be possible to measure the angular Einstein ring radius θ_E to ~10%. The projected Einstein ring radius $\tilde{r}_E$ should also be measurable to ~10% for the majority of these events by combined observations from the ground and a satellite located in an L2 orbit. Thus, it should be possible to measure the mass of most wide-separation and free-floating planets of Earth mass or less.

Finally, we have discussed three methods for distinguishing between isolated planetary events caused by free-floating and bound planets. These include detecting the primary through the influence of the planetary caustic, through the low-amplitude bump in the light curve from the primary, and through detection of the light from the primary itself. These three methods should allow one to distinguish between bound and free-floating planets for approximately one-third of all events regardless of the planet separation, more than 50% of events with projected separations $\lesssim$20 AU, and essentially all events with separations $\lesssim$13 AU.

Work by C. H. was supported by the Astrophysical Research Center for the Structure and Evolution of the Cosmos of the Korean Science and Engineering Foundation, through the Science Research Center program, and by JPL contract 1226901. Work by B. S. G. was supported by a Menzel Fellowship from the Harvard College Observatory. Work by J. H. A. was supported by a grant from the Leverhume Trust Foundation. Work by A. G. was supported by JPL contract 1226901 and NSF grant 02-01266.

REFERENCES

Agol, E. 2003, ApJ, 594, 449
Albrow, M., et al. 1998, ApJ, 509, 687
Alcock, C., et al. 1996, ApJ, 463, L67
Bennett, D. P., & Rhie, S. H. 2002, ApJ, 574, 985
Bennett, D. P., et al. 2004, AAS DPS Meeting, 36, 35.09
Bond, I. A., et al. 2002, MNRAS, 333, 71
———. 2004, ApJ, 606, L155
Chang, K., & Refsdal, S. 1979, Nature, 282, 561
———. 1984, A&A, 132, 168
Di Stefano, R., & Scalzo, R. A. 1999a, ApJ, 512, 564
———. 1999b, ApJ, 512, 579
Dominik, M. 1998, A&A, 333, L79
———. 1999, A&A, 349, 108
Gould, A., & Gaucherel, C. 1997, ApJ, 477, 580
Gould, A., Gaudi, B. S., & Han, C. 2003, ApJ, 591, L53
Gould, A., & Loeb, A. 1992, ApJ, 396, 104
Gould, A., & Welch, D. L. 1996, ApJ, 464, 212
Griest, K., & Safizadeh, N. 1998, ApJ, 500, 37
Han, C., Chung, S.-J., Kim, D., Park, B.-G., Ryu, Y.-H., Kang, S., & Lee, D. W. 2004, ApJ, 604, 372
Han, C., & Gould, A. 1995, ApJ, 447, 53
———. 2003, ApJ, 592, 172
Han, C., & Kang, Y. W. 2003, ApJ, 596, 1320
Holtzman, J. A., Watson, A. M., Baum, W. A., Grillmair, C. J., Groth, E. J., Light, R. M., Lynds, R., & O'Neil, E. J., Jr. 1998, AJ, 115, 1946
Mao, S., & Paczyński, B. 1991, ApJ, 374, L37
Paczyński, B. 1986, ApJ, 304, 1
Rhie, S. H., et al. 2000, ApJ, 533, 378
Soszyński, I., et al. 2001, ApJ, 552, 731
van Belle, G. T. 1999, PASP, 111, 1515
Witt, H. J. 1990, A&A, 236, 311
Witt, H. J., & Mao, S. 1995, ApJ, 447, L105
Yoo, J., et al. 2004a, ApJ, 603, 139
———. 2004b, ApJ, 616, 1204